Separation and Concentration without Clogging Using a High-Throughput Tunable Filter

E. J. Mossige* and A. Jensen
Department of Mathematics, University of Oslo (UiO), P.O. Box 1053 Blindern, N-0316 Oslo, Norway

M. M. Mielnik
Department of Microsystems and Nanotechnology (MiNaLab), SINTEF Digital, P.O. Box 124 Blindern, N-0314 Oslo, Norway

(Received 21 April 2017; revised manuscript received 5 February 2018; published 7 May 2018)

We present a detailed experimental study of a hydrodynamic filtration microchip and show how chip performance can be tuned and clogging avoided by adjusting the flow rates. We demonstrate concentration and separation of microspheres at throughputs as high as 29 ml/min and with 96% pureness. Results of streakline visualizations show that the thickness of a tunable filtration layer dictates the cutoff size and that two different concentration mechanisms exist. Particles larger than pores are concentrated by low-velocity rolling over the filtration pillars, while particles smaller than pores are concentrated by lateral drift across the filtration layer. Results of microscopic particle image velocimetry and particle-tracking velocimetry show that the degree of lateral migration can be quantified by the slip velocity between the particle and the surrounding fluid. Finally, by utilizing differences in inertia and separation mode, we demonstrate size-based separation of particles in a mixture.

DOI: 10.1103/PhysRevApplied.9.054007

I. INTRODUCTION

Microfluidic separation devices have applications in the medical and biological industries, e.g., the concentration of microalgae [1,2] and blood cells [3], and in diagnostics [4,5]. In the early days of microfluidic separation, cross-flow filtration was a popular separation technique [6], where the particle cutoff size is given by the filter size. Cross-flow filters are scalable and easy to manufacture but suffer from clogging, which reduces the separation efficiency and reliability. In the search for a clog-free configuration, Yamada and Seki [7] introduced hydrodynamic filtration in which the flow field was used to control the particle cutoff size instead of the pore size of the filter. Recently, the same authors improved their initial geometry by using slanted channels [8]. Hydrodynamic filters are cheap and parallelizable and have become commercially available, e.g., for blood cell enrichment [9]. However, these filters suffer from low pureness of the processed streams and are restricted to low flow velocities, which limits the throughput.

High throughput can be achieved by utilizing fluid inertia to focus particles on different equilibrium positions based on size [10] or shape [11]. The particles are eventually separated by guiding the focused particle sheets through different outlets. Lim *et al.* separated particles at 50 ml/min in a relatively narrow 80-μm square channel [12]. Despite the high throughput potential, inertial separation devices require high pressures to pump the fluid through long and narrow channels.

The Trilobite microfluidic chip presented in this paper was used previously for the concentration of microalgae [13] and cancer cells [14]. Recently, Mossige *et al.* demonstrated how the flow can be tuned to precisely control the particle cutoff size and concentration ratio [15]. However, only tracer particles were used, and the technology was not demonstrated for separation by using real separation particles.

In this paper, the microfluidic chip is used to separate and concentrate spheres (18, 24, 30, and 69 μm) continuously and at high throughput. By means of streakline visualizations and by measurements of particle concentrations and flow rates, the flow is optimized to maximize the concentration ratios and to avoid clogging.

Two different separation mechanisms are identified for spheres: separation by migration along a porous wall and separation by lateral migration away from this wall. The former is used for the separation and concentration of particles larger than the pores with high concentration ratios, while the latter is used to concentrate small particles, even smaller than the pores. Finally, we present flow-field velocities by microscopic particle image velocimetry

*Also at Trilobite Microsystems A/S, Torridalsveien 21A, 4630 Kristiansand, Norway.
endrejm@math.uio.no

 © 2018 American Physical Society

(μ-PIV) and particle velocities by particle-tracking velocimetry (PTV) to explore the separation and concentration mechanism in detail.

II. SEPARATION PRINCIPLE

The particle separation and concentration is performed by trilobite-shaped separation units; see Fig. 1. These units consist of a solid wall and a permeable wall with turbine-blade-shaped pillars which serve to block out and prevent particles from entering the permeate. The distance between these pillars is 25 μm.

An incoming flow of fluid and particles is split into two streams by the separation unit; the permeate stream, which is directed through the permeate outlet, and the concentrate stream, which carries the particles to a concentrate outlet downstream of the separation units. The permeate stream contains few or no particles, and the removal of permeate liquid leads to increased particle concentration in the concentrate stream. With a mixture of particles in the inflow, the permeate stream contains only particles that are smaller than the distance between pillars.

In Fig. 1(a), the fluid velocity is low, and the particles separate from the permeate stream by migration along the permeable wall. The particles interact with this wall without blocking the pores. Low flow velocities lead to a thick flow layer that ends up as permeate, seen as the dotted streamline and denoted as T_p in the figure. The thick flow layer leads to the high flux of permeate through the permeate outlet, and therefore to high concentration ratios. Separation of smaller particles requires higher fluid velocities; see Fig. 1(b). When the fluid velocity increases, the particles separate from the permeate stream by lateral migration away from the permeable wall instead of migration along it. With this separation principle, it is possible to separate particles which are smaller than the distance between pillars (25 μm) from the permeate stream. However, the velocity increase from Fig. 1(a) to Fig. 1(b) leads to a reduction of T_p, and thus to lower concentration ratios. Therefore, the large particles in Fig. 1(a) can be separated at higher concentration ratios than the small particles in Fig. 1(b).

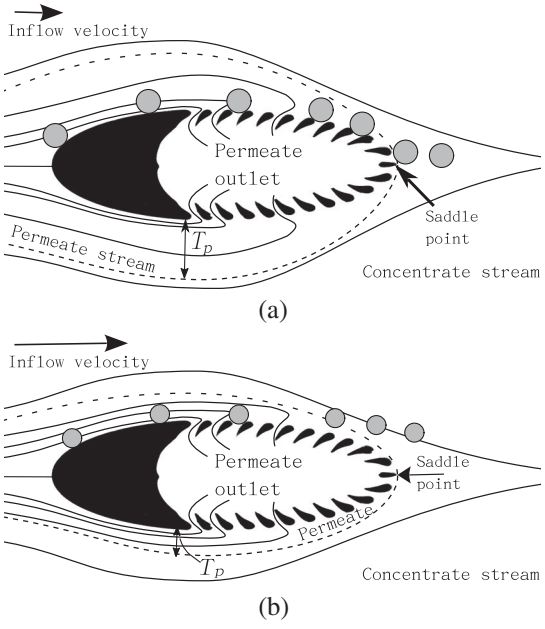


FIG. 1. (a) The trilobite-shaped separation unit. Two different separation principles are shown. In (a), the large particles migrate along the permeable wall and separate without blocking the pores. In (b), the inflow velocity is increased, and the particles separated by lateral migration away from the permeable wall. The flow in (a) is used to separate large particles at high concentration ratios, and the flow in (b) is used to separate particles smaller than the gap width between the pillars (25 μm).

The combination of the uniform inflow and the permeate outflow leads to a saddle point which, in Fig. 1, sits directly downstream of the last pillar. However, the saddle point can be moved downstream by increasing the flow of permeate. This increases the concentration ratio but hinders separation because of the strong suction force exerted by the permeate outlet. For particles larger than the pores, this configuration leads to clogging. For particles smaller than the pores, this configuration leads to an increase in the particle flux through the permeate outlet, and therefore to reduced pureness of the permeate stream.

When the saddle point is moved upstream of the last pillar, the permeate stream is directed back into the main channel, which reduces the concentration ratio. Therefore, the best saddle-point position is immediately downstream of the last pillar. This topic was also discussed in our recent article [15].

III. EXPERIMENTS

A. Experimental setup

A schematic of the experimental setup is shown in Fig. 2. Central to the setup is a pressure system (MFCS-EZ, Fluigent), which is used to control the throughput Q_{in} and permeate flow rate Q_p by adjusting the pressures in the respective reservoirs. The inlet flow Q_{in} is simply the sum of the two outlet flows, $Q_{\text{in}} = Q_p + Q_c$, where Q_c is the flow of concentrate, which is collected in an atmospheric pressure reservoir. A pressure increase in the inflow reservoir leads to an increase in Q_{in}, and a pressure decrease leads to a reduction in Q_{in}. The pressure in the permeate reservoir is primarily adjusted to modify the position of the saddle point. With a pressure increase, the saddle point moves upstream due to a reduction in Q_p. Likewise, with a pressure decrease, the saddle point moves downstream due to an increase in Q_p. The concentrate flow rate Q_c and the permeate flow rate are measured using laboratory scales (Mettler Toledo, ML303T) and are continuously monitored to check for potential fluctuations. The flow rates are easily reproduced because the flow rates are linear functions of the reservoir pressures.

To get rid of gas cavities and bubbles, the flow system is flushed prior to each experiment by applying a high inlet pressure. A low permeate reservoir pressure is applied to create a high suction force through the permeate outlet.

The flow fields and particle separation regimes are characterized by streakline visualizations and by fluid and particle velocimetry (μPIV and PTV, respectively). Fluorescent tracer particles (Life Technologies, 1 μm, Carlsbad, California) that accurately follow the flow are used to visualize the flow fields, particularly around the saddle point, and for flow velocity measurements. Fluorescent polymer spheres (Cospheric, Santa Barbara, California) with mean diameters of 21, 24, 32, and 69 μm are used as separation particles and for velocity measurements by PTV. These particles are listed in Table I. A continuous light source (Olympus U-HGLGPS) is used in combination with a filter set for green light excitation (ZET532/10x, Chroma) to illuminate these fluorescent particles. Objectives with magnifications of 10× (Olympus Plan C N $10\times/0.25$) and 20× (Olympus UPlanFL N $20\times/0.50$) are used for the visualizations, and images are captured with a CCD camera (PCO, pco.4000) which is mounted onto the upright microscope (BX43, Olympus). For the flow and particle velocity measurements, a double-pulsed Nd:yttrium-aluminum-garnet (YAG) laser (Litron nano PIV) is used as the light source (wavelength 532 nm, i.e., green light) and the time difference between the two successive laser pulses is controlled with a LabVIEW program, typically 6 μs. The 20× objective is used for all of the velocity measurements, and the particle image pairs are processed with a homemade ensemble average PIV algorithm to extract the flow velocity fields. A thresholding technique is applied to extract the particle velocities from the same images, which are captured at the center plane, halfway between the channel bed and the glass lid. Owing to the low particle concentrations, about one particle per three exposures, the images are stacked on top of each other to synthetically increase the number of particles in each image used for the PTV calculations.

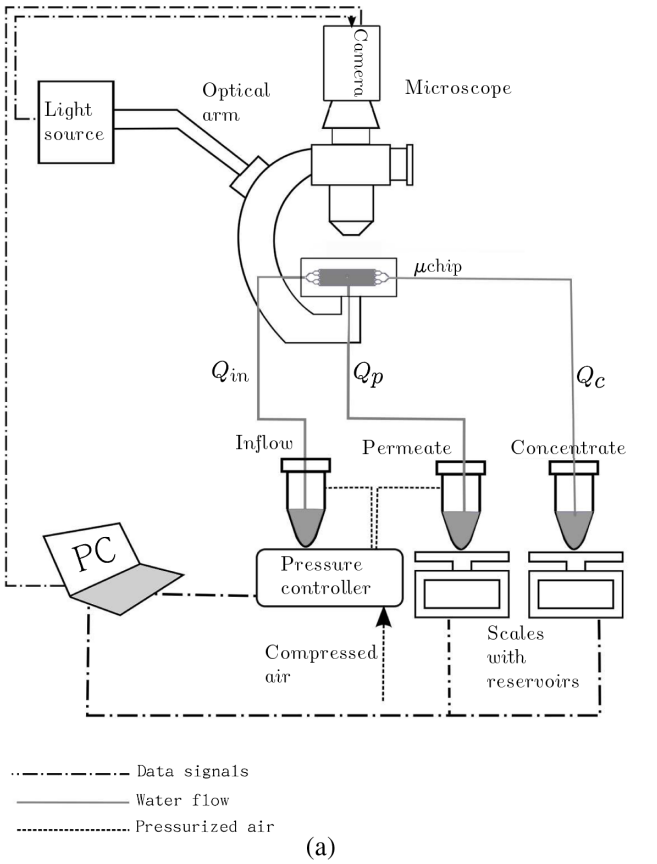
The particle concentrations are determined by counting the number of particles in 2-μl drops, dispersed onto a microscope slide and viewed through a 4× objective (Olympus Plan C N $4\times/0.10$).

TABLE I. Separation particles and tracer particles used in the experiments.

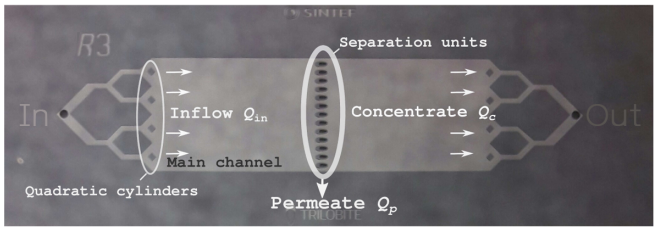
Separation particles					Tracers
Group	Small		Large		⋯
Diameter (D_p)	18 μm	24 μm	30 μm	69 μm	1 μm
Reference name	D_{p18}	D_{p24}	D_{p30}	D_{p69}	⋯
Concentration $\times 10^5$ (vol %)	1.71	8.57	8.57	6.86	1.14
Density (g/cm^3)	1.0	1.0	1.0	1.0	1.05
Excitation (nm)	300–600	300–600	300–600	300–600	450–580

B. Microfluidic chips

The microfluidic chips, see Figs. 2 and 3, were manufactured by SINTEF Mi Na Lab using standard micromachining processes. The process is described in Ref. [15]. In the chip layout presented in this paper, an array of 13 trilobite units, 460 μm wide and 1155 μm long, makes up the separation section in the 90-μm-deep main channel. With 740 μm from center to center, these units block 62%

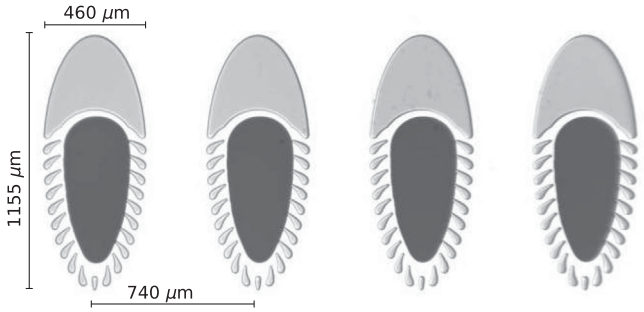


(a)

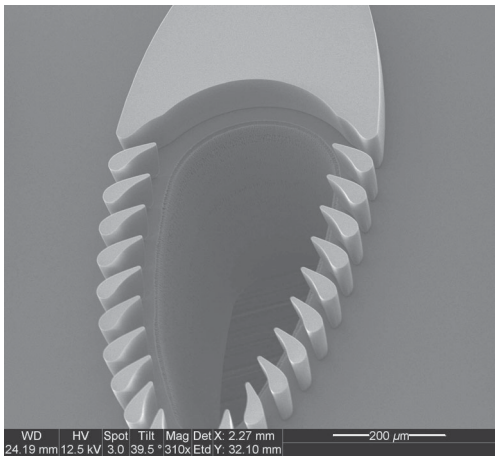


(b)

FIG. 2. (a) Experimental setup. A pressure system and laboratory scales are used to control the flow rates Q_{in}, Q_p, and Q_c. The particles are illuminated with continuous light for the streakline visualizations, and with a pulsed Nd:YAG laser for the μPIV and PTV measurements. (b) Microfluidic chip. The main channel is 30 mm long, 10 mm wide, and 90 μm deep, with 13 separation units.



(a)



(b)

FIG. 3. (a) An enlargement of four separation units, rotated 90°. Each unit is 460 μm wide and 1155 μm long, and the distance from center to center is 740 μm. (b) SEM image of a single separation unit.

of the channel cross-section area. Branching channels connect the inlet and the concentrate outlet to the main channel, which is 10 mm wide and 30 mm long.

The high pressure drop resulting from abrupt changes in the fluid volume can cause the liquid to degas. This degassing, in turn, can lead to bubble formation. To reduce the pressure drop in the entrance region to the main channel, quadratic cylinders are placed upstream and downstream to effectively remove this problem.

A 300-μm-thick glass slide is bonded onto the fluidic chip for sealing and viewing purposes. The chips are cleaned between each experimental run by using a syringe to flush the channels with acetone, propanol, and deionized water. In addition, piranha solution (sulfuric acid to hydrogen peroxide 3∶1; CAUTION: highly corrosive and dangerous to the skin) is injected into the channels. A glass syringe is used for the injection since the strong piranha solution does not dissolve glass. For details on the piranha preparation procedure, see, e.g., Ref. [16].

The inlet and the outlets on the chip are connected to the reservoirs by tubing and a homemade chip holder machined in acrylic glass. The inlet and the concentrate outlet on the chip holder are circular (1-mm diameter), while the permeate outlet, shared by all of the trilobite separation units, is a rectangular channel (1 × 10 mm).

C. Particles

The microspheres used to study separation and for velocity measurements by PTV are called "separation particles" and are referred to in the text as D_{p18}, D_{p24}, D_{p30}, and D_{p69}, respectively. D_{p18} and D_{p24} are referred to as small particles, and D_{p30} and D_{p69} are referred to as large particles. These neutrally buoyant particles (1 ± 0.01 g/cm^3) are dispersed in deionized water at 25 °C. An overview of the different particles used in this work is shown in Table I.

Tracer particles (1-μm mean diameter), used for μPIV and for fluid flow visualizations, are mixed with the separation particle solutions to a concentration ratio of 1.14×10^{-5} by volume. The surfactant Triton-X (Sigma Aldrich) is added to the particle solutions to prevent bubble formation and particle agglomeration to the walls and the coverslip surface.

IV. RESULTS

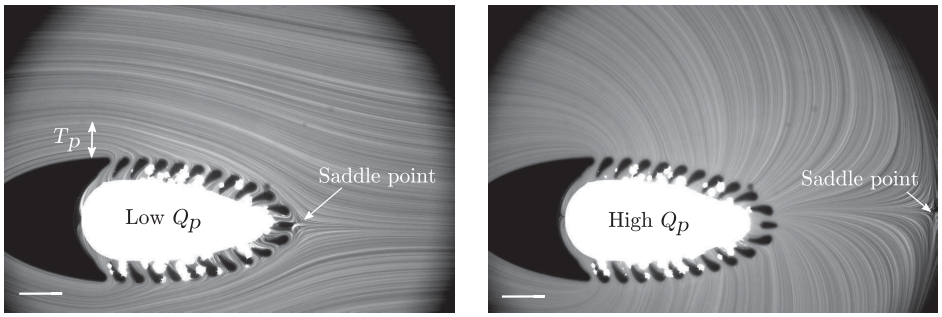
A. Separation phenomena and performance

1. Calibration of the system without particles

In order to determine the flow rates, Q_{in} and Q_p, which give the desired position of the saddle point and extent of flow layer T_p, the system is calibrated by streakline visualizations using tracers. Our results show that an increase in the throughput Q_{in} leads to an increase of permeate, Q_p, when the pressure in the permeate reservoir is kept constant. As a consequence of the increased suction, the saddle point moves downstream. Likewise, a decrease in Q_{in} leads to a reduction of permeate, which is followed by an upstream displacement of the saddle point. Figure 4 shows streakline visualizations of an upstream [Fig. 4(a)] and downstream [Fig. 4(b)] saddle point.

To keep the saddle point fixed when Q_{in} changes, Q_p has to be altered by adjusting the pressure in the permeate reservoir. The saddle point is moved upstream by increasing the pressure in the permeate reservoir (which reduces the permeate flux) and moves downstream by decreasing the pressure in the permeate reservoir (which increases the permeate flux).

The flow layer T_p also varies with Q_{in}. When the saddle point is fixed near the last pillar, an increase in the inflow leads to a reduction of T_p. In our recent article [15], where tracers but no separation particles were used, it was hypothesized that the layer thickness can be used to manipulate the particle cutoff size. It was postulated that the particle center of mass must be outside the permeate layer for successful separation; it would then be carried by the concentrate flow, away from the filtration pillars. To



(a) (b)

FIG. 4. Streaklines obtained using tracer particles using a single trilobite unit show (a) an upstream saddle point resulting from low suction Q_p and (b) a downstream saddle point resulting from high suction Q_p. The flow field in (a) is generated by applying a high permeate reservoir pressure, while the flow field in (b) is generated by applying a low permeate pressure. In (a), T_p is small, which enables separation, while in (b) T_p is larger (it extends outside the field of view of the image), which hinders separation. The white dots are an agglomeration of dust and tracer particles, but these particles do not influence the flow. The scale bar is 100 μm.

ensure this clog-free behavior, the particle must be at least twice the size of the filtration layer. For spheres, this requirement yields $D_p > 2T_p$.

Our measurements show that the pressure-driven flow fields are stabilized by increasing the flow rates. This is the case because a pressure increase in the reservoirs leads to a dampening of the pressure fluctuations. For the flow field used for separation, the magnitude of the fluctuations is less that 1%, scaled by the mean pressures in the reservoirs. Correspondingly, the fluctuations in flow rates are also 1%, measured by laboratory scales. By applying the maximum pressure (7 bar) available for our system, the highest throughput achievable is 32 ml/ min.

After calibration, the flow fields are easily reproduced by imposing precalibrated pressures, with only 1% variation between experiments.

The permeate outlets on the Trilobite separation units are connected to each other via a shared outlet channel for the permeate fluid. The pressure drop required to push the fluid through this channel and into the tubing (that connects the fluidic chip to the permeate reservoir) leads to a slight variation in the pressures at the different permeate outlets. Naturally, this pressure variation leads to a variation in the saddle-point positions across the array of separation units. To avoid clogging, the flow is adjusted such that the saddle points are never downstream of the last pillar for any of the separation units.

2. Separation regimes and influence of saddle-point position

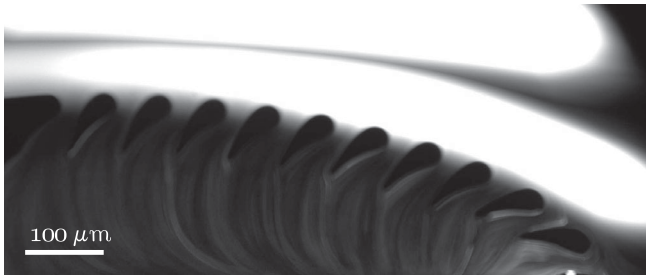
The streakline visualizations in Fig. 5 illustrate the two different separation mechanisms we observe for the Trilobite filter, namely, wall and lateral migration. The separation particles create the thick streaks, and the tracers create the thin streaks used to visualize the fluid flow. In Figs. 5(a) and 5(b), the particles are larger than the pores and separate from the permeate flow by wall migration at low fluid velocities. In Figs. 5(c) and 5(d), the particles are smaller than the pores and separate by lateral migration at high fluid velocities.

The streakline visualizations in Fig. 6 show how the saddle-point position dictates the separation performance. In Fig. 6(a), the saddle point is immediately downstream of the last pillar, which leads to the successful separation of 18-μm particles. However, when the saddle point is moved downstream [Fig. 6(b)], these particles cannot separate from the permeate due to the high permeate suction. As a result, the particles follow the streamlines into the permeate outlet. In Fig. 6(c), the saddle point is still downstream of the last pillar; however, now the particles are larger than the pores. This configuration immediately leads to clogging, which, in turn, pushes the saddle point even farther downstream. The repositioning modifies the flow field, directing the flow inwards towards the pillars. This modification of the flow further suppresses separation and amplifies the clogging, as seen in Fig. 6(d).

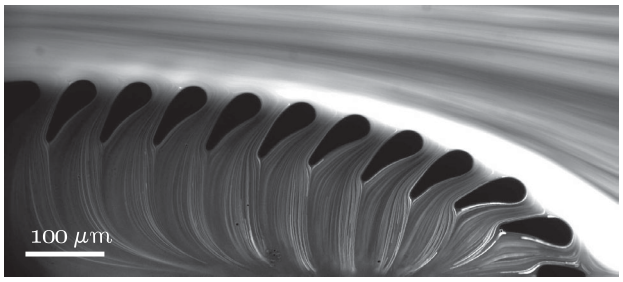
The presence of separation particles does not affect the flow rates when clogging does not occur. In particular, the injection of particles does not influence the position of the saddle point, as seen in Figs. 6(a) and 6(b). When clogging occurred, however [Figs. 6(c) and 6(d)], the flow rates are reduced. By monitoring the flow rates, it is therefore possible to detect clogging without the need for visual inspection.

3. Concentration and filtration performance

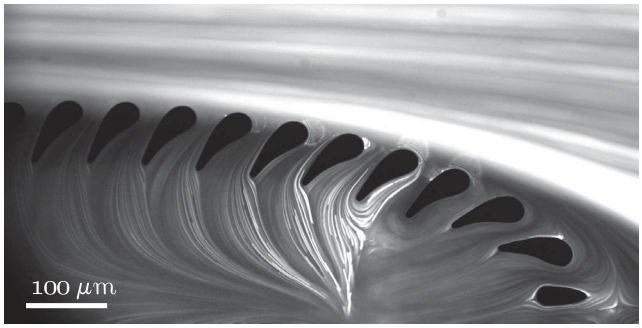
The concentration ratio φ_c is the ratio of particle concentrations in the concentrate, C_c, to the particle concentration in the inflow, C_{in}. Maximization of the concentrate ratio is achieved through maximizing the permeate flux ratio, defined as $Q_p^* = Q_p/Q_{\text{in}}$. In the experiments, this maximization is done by finding the minimum inflow Q_{in} required to separate each type of particle (18, 24, 30, and 69 μm). The permeate flux is adjusted to fix the saddle point near the last pillar.



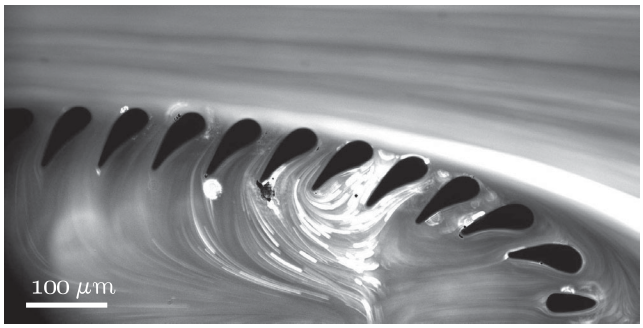
(a) $D_p = 69\ \mu\text{m}$, $Q_{in} = 10\ \text{ml/min}$



(b) $D_p = 30\ \mu\text{m}$, $Q_{in} = 18\ \text{ml/min}$

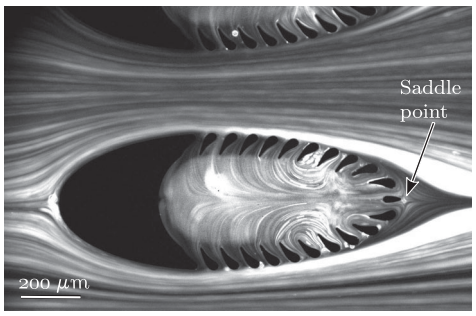


(c) $D_p = 24\ \mu\text{m}$, $Q_{in} = 32\ \text{ml/min}$

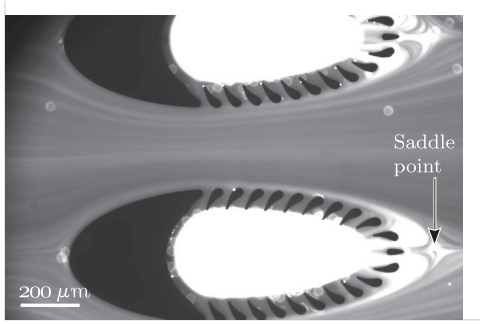


(d) $D_p = 18\ \mu\text{m}$, $Q_{in} = 32\ \text{ml/min}$

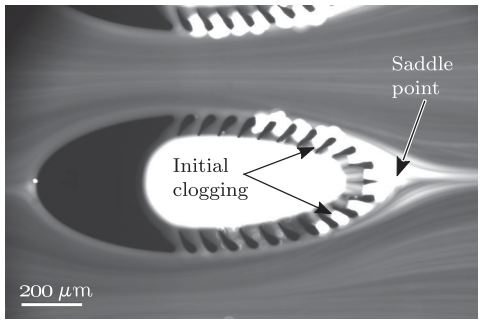
FIG. 5. Streaklines that show the different separation mechanisms. The separation particles create the thick streaks, and the tracers create the thin streaks used to visualize the fluid flow. The large particles, (a) 69 μm and (b) 30 μm, separate from the permeate flow by migration along the wall at low fluid velocities. Refer to the Supplemental Material [17] for a movie of the latter. The small particles, (c) 24 μm and (d) 18 μm, separate from the permeate flow by migration across the streamlines of the flow at high fluid velocities. The saddle point is located directly downstream of the last pillar.



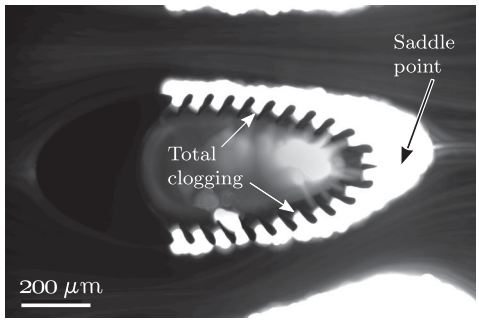
(a)



(b)



(c)



(d)

FIG. 6. Streakline visualizations that show the importance of a correct saddle-point position. The flow in (a) has a saddle point near the last pillar, seen as converging streaklines produced by the tracer particles. The particles (18 μm) separate successfully from the permeate flow because the saddle point is sufficiently far upstream. In (b), the saddle point is moved downstream and the particles no longer separate from the flow. Instead, they end up in the permeate outlet. In (c) and (d), the particles are larger than the pore size and clog the permeable wall because the saddle point is too far downstream.

TABLE II. Flow rates and performance parameters for particles with diameters D_p. Q_{in} is the minimum influx and Q_p is the maximum permeate flux that ensures separation. The ratio Q_p/Q_{in} the permeate flux ratio Q_p^*. φ_p is the filtration ratio and φ_c is the concentration ratio.

	Flow rates			Performance	
D_p	Q_{in}	Q_p	Q_p^*	φ_c	φ_p
D_{p18} (18 μm)	32.0	2.6	0.08	1.04	0.43
D_{p24} (24 μm)	32.0	2.6	0.08	1.08	0.96
D_{p30} (30 μm)	18.8	2.9	0.15	1.18	1.00
D_{p69} (69 μm)	10.1	3.0	0.29	1.42	1.00
Unit	(ml)/ min	(ml)/ min	...	...	...

Table II is a list of the minimum flow rates required for separation, Q_{in}, the permeate flux, Q_p, and the maximum permeate flux ratio, Q_p^*. Attempting to increase Q_p^* above these maximum values leads to clogging because it can be achieved only by moving the saddle point downstream of the last pillar. Our results show that Q_p^* increases with particle size. This is the case because the separation of large particles can be performed at low flow rates Q_{in}, and because the low throughput does not lead to a reduction in Q_p. The reason why large particles can be separated at low velocities is that lateral migration is not necessary. For instance, 10 ml/ min is sufficient to separate D_{p69}, while a threefold increase to 32 ml/ min is required to induce the lateral migration required to separate D_{p18} from D_{p24}.

Along with the flow rates, measures of concentration and filtration performance are presented in Table II. The filtration ratio φ_p is a measure of the pureness of the permeate stream and is defined as $\varphi_p = 1 - [(C_p)/(C_{in})]$, where C_p is the particle concentration in the permeate and C_{in} is the particle concentration in the inflow. For D_{p18}, the filtration ratio φ_p is 0.43, and for D_{p24}, the filtration ratio is as high as 0.96; i.e., the permeate particle concentration is only 4% of the inflow particle concentration. Since D_{p30} and D_{p69} are larger than the gaps between the pillars (25 μm), they cannot enter the permeate; hence, $\varphi_p = 1$.

High pureness is important in purification processes such as the removal of contaminants to produce drinking water. In these types of processes, only a very low concentration of particles can be accepted in the stream used for drinking water, as contaminants could be harmful and could lead to disease. In other words, φ_p in the permeate stream must be lower than some threshold. By looping the permeate stream, higher pureness is possible for particles smaller than the gap width.

For D_{p18}, the increase in particle concentration is 4% from inlet to concentrate outlet, while for D_{p69}, the increase is as much as 42%. The reason why the separator performs better for the large particles is that the permeate flux ratio Q_p^* increases with size, and that all of the particles are concentrated, i.e., $\varphi_p = 1$.

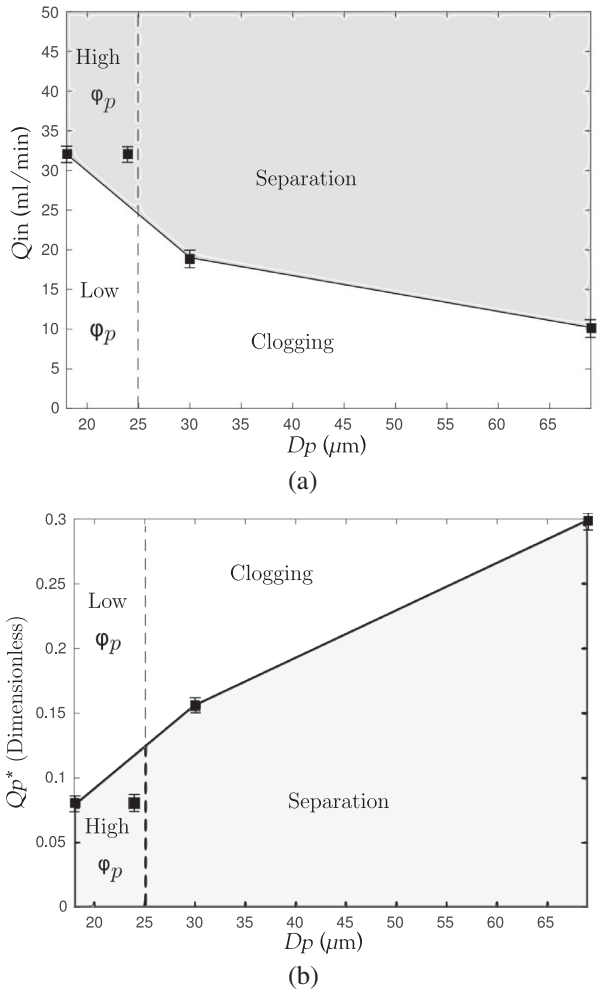


FIG. 7. Separation and clogging regimes for particles with diameters D_p (x axis) with (a) minimum inflow Q_{in} and (b) maximum permeate flux ratio Q_p^*. The plots show that large particles (>25 μm) can be separated at (a) lower flow rates Q_{in} and (b) higher permeate flux ratios Q_p^* than small particles (<25 μm). The dotted line indicates the pore size (25 μm). High φ_p indicates at least 43% pureness, i.e., $\varphi_p > 43\%$. This is the pureness obtained for D_{p18} with the highest flow rate available with the setup (32 ml/ min). Low φ_p indicates $\varphi_p < 43\%$, which is the case if the flow rate is reduced below 32 ml/min or the saddle point is moved downstream. The mass-flow fluctuations from the mean of each experiment as well as the variation of the mean mass flow between experiments is 1%, shown by the error bars.

High concentration ratios are crucial in many industrial and medical applications. In industrial bioengineering processes, such as in microalgae harvesting, a high concentration of algae is required to get a usable product. In medical applications such as the study of live cells under the microscope, a dense population of cells is important in order to obtain statistically significant results. For our device, the concentration ratio can be increased by looping the concentrate flow or by adding separation units downstream or upstream of the existing row of separation units.

The same can be achieved with a series arrangement of microfluidic chips.

Figure 7 shows separation and clogging regimes for particles with diameters D_p (the x axis). The minimum inflow Q_{in} that ensures separation is plotted in Fig. 7(a), and the maximum permeate flux ratio Q_p^* is plotted in Fig. 7(b). "High φ_p" indicates at least 43% pureness, i.e., $\varphi_p > 43\%$, which is the pureness for D_{p18}, and "low φ_p" indicates $\varphi_p < 43\%$. The plots show that large particles can be separated at lower flow rates Q_{in} and higher permeate flux ratios Q_p^* than small particles, and that both D_{p18} and D_{p24} are separated by high pureness φ_p, i.e., $\varphi_p > 43\%$. The error bars indicate the mass-flow variation, which is 1%.

B. Flow-field and particle velocities

1. Flow-field velocities

Figure 8 shows a vector plot of the velocity fields used to concentrate the spheres larger than the pores, D_{p69} [Fig. 8(a)] and D_{p30} [Fig. 8(c)]. The circles indicate the particle size, and the solid line is the thickness of the permeate flow layer. Figures 8(b) and 8(d) show flow details around the particles. The velocity increase from Figs. 8(a)–8(c) leads to a thinning of the permeate layer due to the decrease in permeate flux.

In our previous article [15], it was hypothesized that the particle center of mass must be outside the permeate layer for successful separation, which yields $D_p > 2T_p$ as the minimum cutoff. This hypothesis was based on the results of streakline visualizations and PIV velocimetry using tracers. However, our measurements using separation particles show that $D_p > 2T_p$ is too strict and that separation is possible for particles comparable in size to the separation layer, i.e., $D_p > T_p$. This principle is shown in Fig. 8, where T_p is 60 μm for 69-μm spheres [Fig. 8(a)], and 32 μm for 30-μm spheres [Fig. 8(b)]. This new knowledge means that smaller particles can be separated than was postulated in Ref. [15] and that higher concentration ratios can be achieved.

Figures 8(b) and 8(d) show that the particle size is comparable to the thickness of a shear layer, which, in turn, is comparable to the permeate thickness. Particles inside this layer experience a strong velocity gradient, which induces rotation. The resulting rolling over the porous wall prevents clogging.

2. Particle velocities

Figure 9 shows the particle (the red vectors) and fluid-flow velocities (the black vectors) taken in the particle center of mass, under the flow conditions given in Table II. In Figs. 9(a) and 9(b), the particles (D_{p69} and D_{p30}, respectively) are larger than the pores and migrate along the pillars at low velocities. In Fig. 9(a), the three leftmost particles (D_{p69}) are inside the permeate layer. The particle velocities can be easily distinguished from the fluid

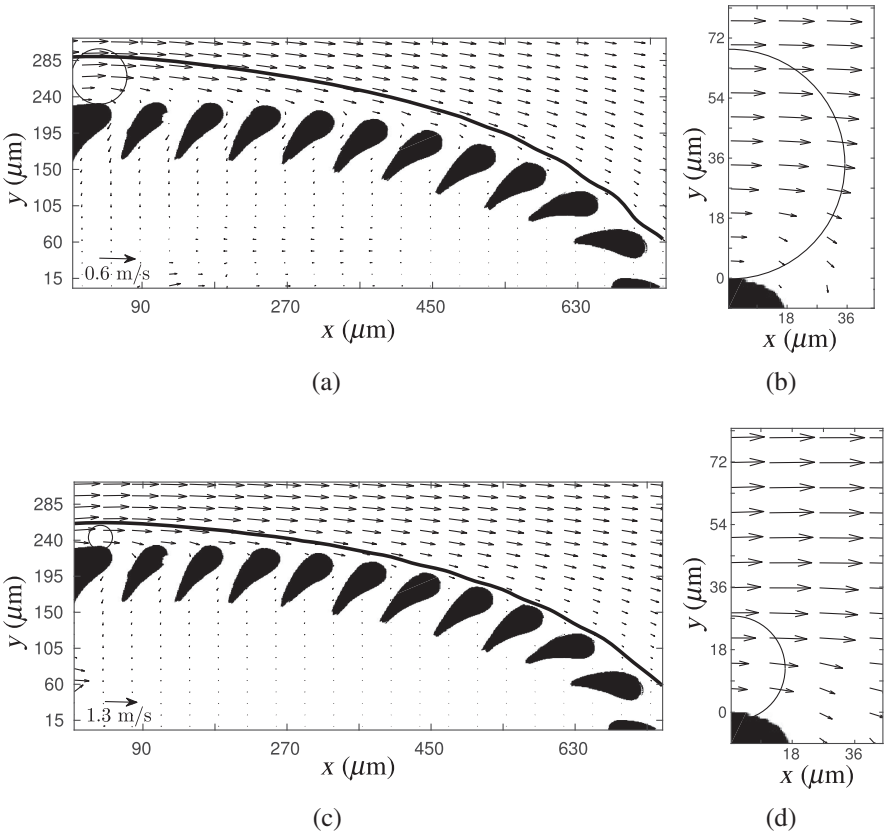


FIG. 8. Vector plots of velocity fields used to separate (a),(b) D_{p69} and (c),(d) D_{p30}, where (b) and (d) are enlarged views around the particles. The circles indicate the typical particle size, and the solid line is the permeate streamline. The particles are comparable in size to the permeate layer thickness in (a) and (c), which is the cutoff size; $D_p > T_p$. The particles are also comparable in size to the shear layer thickness in (b) and (d).

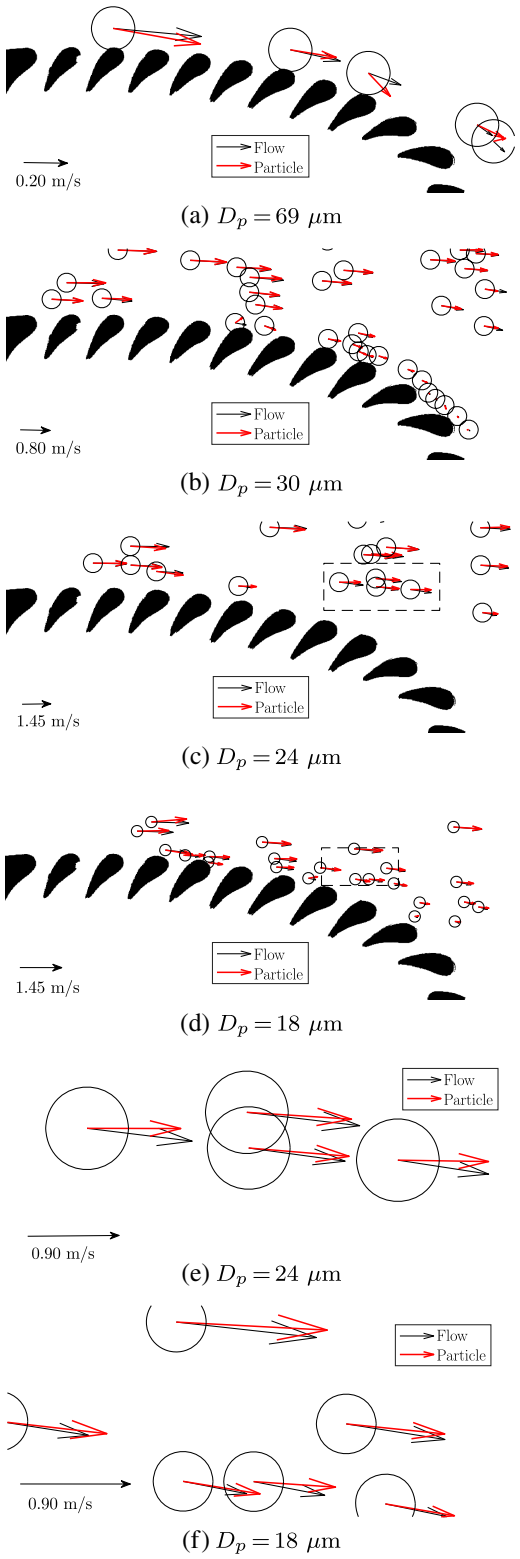


FIG. 9. Particle vectors (red) and flow velocity vectors in the center of the particle (black). The large particles in (a) and (b) separate at low velocities by migration along the wall, whereas the small particles in (c) and (d) separate at high velocities by migration across streamlines. The enlarged views in (e) and (f) show that the particle velocity vectors in (c) and (d) are directed more outwards, away from the wall, than the corresponding fluid velocities.

velocities and are directed more inwards, towards the filtration pillars. This is an indication of rolling over the wall due to the shear within the permeate layer. The two rightmost particles are outside this layer, which shrinks with downstream distance along the pores. Since they get associated with streamlines in the concentrate flow, their velocities are directed away from the permeable wall. Thus, since the particles are much larger than the thin permeate layer in the downstream region, they experience some degree of lateral displacement. However, this is a size effect and is not due to inertia. Figure 9(b) shows velocities of D_{p30}. Compared to the situation in Fig. 9(a), the particles in the downstream region are much closer to the pillars. This is the case because the centers of these particles are inside the permeate layer. Thus, their velocities are also much more similar to the corresponding fluid velocities than in Fig. 9(a), as these particles experience no lateral migration under the current flow conditions.

In Figs. 9(c) and 9(d), the particles (D_{p24} and D_{p18}, respectively) are smaller than the pores. Compared to the rolling regimes in Figs. 9(a) and 9(b), fewer particles are observed in the region directly downstream the filtration structures. This effect is due to migration across streamlines. Because this migration is induced by inertia, it is particularly effective in regions of high streamline curvature, such as near the saddle point. The effect is also more pronounced for larger particles, as evidenced by fewer particles in the vicinity of the filtration structure in the downstream region for D_{p24} as compared to D_{p18}. This difference in the degree of lateral migration also explains the difference in separation efficiency between the two particle sizes; 96% vs 43% pureness.

Finally, Figs. 9(e) and 9(f) are enlarged views of the regions inside the dashed rectangles in Figs. 9(c) and 9(d). These figures show clearly that the particle velocities are directed outwards compared to the corresponding fluid velocities. Again, this difference between the direction of the fluid and particle velocities shows particle migration across the streamlines.

Theoretically, this tendency to migrate can be rationalized by considering the slip Reynolds number, which is a measure of the amount of inertia in the fluid surrounding the particles. The drag force causes the particles to lag behind the fluid [18], giving rise to the slip velocity $U_s = u_p - U_p$, where u_p is the fluid velocity taken in the geometrical center of the particles and U_p is the corresponding fluid velocity. The slip Reynolds number (Re) is defined as $\mathrm{Re} = U_s D_p \nu^{-1}$, where ν is the kinematic viscosity of the fluid. The slip velocities for D_{p18} and D_{p24} are measured to be 0.4 and 0.5 m/s, which yields Re values of 7 and 13, respectively, indicating stronger inertial migration for D_{p24}, which is in agreement with our experimental observation. Note that the Re cannot be used to differentiate between lateral and wall migration since the latter is a size effect where the movement of particles is

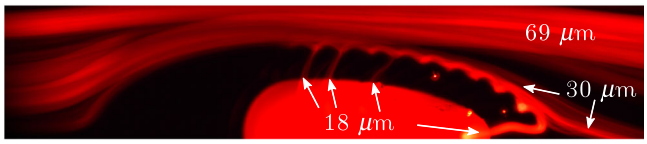


FIG. 10. Simultaneous concentration and separation of 18 μm from 30- and 69-μm spheres, shown by streaklines. The flow rate Q_{in} is 18 ml/ min, which is the velocity required to separate 30-μm spheres by migration along the pillars. The 18-μm spheres follow the flow of permeate through the pillar gaps because the velocity is too low to induce lateral drift away from the pillars. However, the velocity is sufficiently high to induce lateral migration of the largest (69-μm) spheres. Because of the high degree of lateral displacement, these particles can be separated from the 30-μm spheres downstream of the separation units.

dictated by the combination of the flow-induced hydrodynamic forces and the physical obstruction caused by the filtration pillars.

C. Separation of particles by size

Our results with individual particles indicate that size-based separation in a mixture is possible. In order to verify this possibility, we perform a separation of particles larger than pores from particles smaller than pores. Figure 10 is a streakline visualization of size-based separation of 30- and 69-μm spheres from 18-μm spheres. Because of the dewatering through the permeate outlet, the large particles are simultaneously concentrated. With the employed flow rate, 18 ml/ min, the flow velocity is sufficiently high to induce rolling over the pillars and to avoid clogging for D_{p30}. However, the flow rate is too low to induce lateral drift away from the pillars for D_{p18}. Therefore, these particles follow the flow of permeate through the filtration pores and are thus successfully separated from the large spheres.

The flow velocity is sufficiently high to induce lateral drift for 69-μm spheres. The migration across streamlines is enhanced by the fact that these particles are larger than the permeate flow layer, i.e., $D_p > T_p$, and they therefore get associated with streamlines in the concentrate flow region. As a result, there are no 69-μm particles directly downstream of the separation unit (only 18- and 30-μm ones). The difference in lateral displacement between 30- and 69-μm spheres can be utilized as an alternative separation method for particles larger than pores. By directing the particles through separate outlets downstream of the separation units, efficient fractionation by size is possible.

V. CONCLUSION

Filtration and concentration of rigid spheres without clogging is performed with throughputs as high as 29 ml/ min and with 96% pureness. Two different filtration mechanisms are identified, namely, concentration by particle migration along the permeable wall and concentration by lateral drift across streamlines. The former is used to concentrate particles larger than pores at low slip velocities and with high concentration ratios, while the latter is used to concentrate particles smaller than pores by utilizing inertia. It is found that the cutoff size is given by the permeate layer thickness, which is an improvement on earlier predictions.

The filter performance is found to rely heavily on the saddle-point position. The optimal position of the saddle point is found to be immediately to the rear of the filtration unit. With this position, the clog-free property is conserved, while the concentration ratio is maximized. Moving the saddle point upstream of this position reduces the concentration ratio, while moving it downstream leads to clogging.

By utilizing the difference in inertia and separation mode, we show that the filter can be utilized for efficient size-based separation. This additional functionality is achieved through a combination of direct filtrate-retentate separation and by size-based lateral positioning downstream of the filtration unit.

ACKNOWLEDGMENTS

This project was funded by Trilobite Microsystems A/S and The Research Council of Norway (Project No. 232148). Support was also received from the Norwegian Micro- and Nanofabrication Facility (NORFAB) infrastructure project.

[1] Chih-Chung Chen, Yu-An Chen, Yi-Ju Liu, and Da-Jeng Yao, A multilayer concentric filter device to diminish clogging for separation of particles and microalgae based on size, Lab Chip **14**, 1459 (2014).

[2] Neus Godino, Felix Jorde, Daryl Lawlor, Magnus Jaeger, and Claus Duschl, Purification of microalgae from bacterial contamination using a disposable inertia-based microfluidic device, J. Micromech. Microeng. **25**, 084002 (2015).

[3] M. Sneha Maria, B. S. Kumar, T. S. Chandra, and A. K. Sen, Development of a microfluidic device for cell concentration and blood cell-plasma separation, Biomed. Microdevices **17**, 115 (2015).

[4] Jeonghun Nam, Yong Shin, Justin Kok Soon Tan, Ying Bena Lim, Chwee Teck Lim, and Sangho Kim, High-throughput malaria parasite separation using a viscoelastic fluid for ultrasensitive PCR detection, Lab Chip **16**, 2086 (2016).

[5] Majid Ebrahimi Warkiani, Andy Kah Ping Tay, Bee Luan Khoo, Xu Xiaofeng, Jongyoon Han, and Chwee Teck Lim, Malaria detection using inertial microfluidics, Lab Chip **15**, 1101 (2015).

[6] Andreas Lenshof and Thomas Laurell, Continuous separation of cells and particles in microfluidic systems, Chem. Soc. Rev. **39**, 1203 (2010).

[7] Masumi Yamada and Minoru Seki, Hydrodynamic filtration for on-chip particle concentration and classification utilizing microfluidics, Lab Chip **5**, 1233 (2005).

[8] Masumi Yamada, Wataru Seko, Takuma Yanai, Kasumi Ninomiya, and Minoru Seki, Slanted, asymmetric microfluidic lattices as size-selective sieves for continuous particle/cell sorting, Lab Chip **17**, 304 (2017).

[9] Rainer D. Jäggi, Roger Sandoz, and Carlo S. Effenhauser, Microfluidic depletion of red blood cells from whole blood in high-aspect-ratio microchannels, Microfluid. Nanofluid. **3**, 47 (2006).

[10] Kaitlyn Hood, Soroush Kahkeshani, Dino Di Carlo, and Marcus Roper, Direct measurement of particle inertial migration in rectangular microchannels, Lab Chip **16**, 2840 (2016).

[11] Mahdokht Masaeli, Elodie Sollier, Hamed Amini, Wenbin Mao, Kathryn Camacho, Nishit Doshi, Samir Mitragotri, Alexander Alexeev, and Dino Di Carlo, Continuous Inertial Focusing and Separation of Particles by Shape, Phys. Rev. X **2**, 031017 (2012).

[12] Eugene J. Lim, Thomas J. Ober, Jon F. Edd, Salil P. Desai, Douglas Neal, Ki Wan Bong, Patrick S. Doyle, Gareth H. McKinley, and Mehmet Toner, Inertio-elastic focusing of bioparticles in microchannels at high throughput, Nat. Commun. **5**, 4120 (2014).

[13] Birgitte K. Honsvall, Dag Altin, and Lucy J. Robertson, Continuous harvesting of microalgae by new microfluidic technology for particle separation, Bioresour. Technol.: Biomass, Bioenergy, Biowastes, Convers. Technol., Biotransform., Prod. Technol. **200**, 360 (2016).

[14] Tao Dong, Zhaochu Yang, Qianhua Su, Nhut Minh Tran, Eirik Bentzen Egeland, Frank Karlsen, Yulong Zhang, Matteo Joseph Kapiris, and Henrik Jakobsen, Integratable non-clogging microconcentrator based on counter-flow principle for continuous enrichment of CaSki cells sample, Microfluid. Nanofluid. **10**, 855 (2011).

[15] E. J. Mossige, A. Jensen, and M. M. Mielnik, An experimental characterization of a tunable separation device, Microfluid. Nanofluid. **20**, 160 (2016).

[16] Werner Kern, and RCA critical cleaning process, http://www.microtechprocess.com/pdf/MTS_RCA.pdf (2007).

[17] See Supplemental Material at http://link.aps.org/supplemental/10.1103/PhysRevApplied.9.054007 for the concentration of 30-μm spheres without clogging shown in Fig. 5(b).

[18] Martin R. Maxey and James J. Riley, Equation of motion for a small rigid sphere in a nonuniform flow, Phys. Fluids **26**, 883 (1983).